Acta Cryst. (1999). A**55**, 133–142

Real-space Green's-function approach within RHEED

P. M. Derlet† and A. E. Smith*

Department of Physics, Monash University, Clayton, Victoria 3168, Australia.
E-mail: andrew.e.smith@sci.monash.edu.au

(*Received 19 January 1998; accepted 28 May 1998*)

Dedicated to Professor A. F. Moodie on the occasion of his 75th birthday

Abstract

Green's-function techniques are used to obtain a real-space series solution for the elastic reflection high-energy electron diffraction (RHEED) from a crystalline surface. A renormalized perturbation expansion due to potential self-scattering is developed for the local real-space Green's function. With the Pt (111) surface as an example, numerical results are obtained for reflection coefficients and intensities. In particular, calculations are performed to obtain the local density of states at and near the surface region. Total density-of-states calculations are also performed. These provide a basis for a discussion of the form of resonant electronic Green's functions that can be used to describe the surface resonance phenomenon within RHEED.

1. Introduction

The phenomenon of reflection of high-energy electron diffraction (RHEED) at or near the surface region of a material constitutes an inherently dynamical physical process which precludes the forward-scattering approximation often used to simplify the problem of electrons in transmission. Within the so-called '*n*-rod' scheme to the surface problem, the real-space nature of multiple scattering perpendicular to the surface (the z direction) becomes manifest through the resulting coupled integral/differential equations with respect to the z coordinate and the two-dimensional reciprocal-lattice vectors parallel to the surface. It is the numerical solution to these equations that produces the theoretical RHEED patterns which, in many cases, have so successfully reproduced the experimentally obtained electron diffraction patterns (Smith *et al.*, 1992; Wang, 1996). The numerical realization of the distinctive horizontal Kikuchi lines (due to potential scattering under the Bragg condition) and the resonance parabolae (Peng, 1994; Dudarev & Whelan, 1996) due to the incident electrons accessing semi-bulk material eigen states have lead to preferable scattering geometries that significantly increase the sensitivity of the reflection technique for characterization of surface material properties.

Much work has been performed in the solution of the differential form of the coupled Fourier-transformed one-dimensional Schrödinger equation [see for example Dudarev & Whelan (1996) for a relatively up to date discussion]. Recently, however, there has been increased interest in the solution to the integral form of these equations. This has been motivated primarily by the recent analytical solution of Dudarev & Whelan to the two-rod problem of surface resonance scattering (Dudarev & Whelan, 1994*a*,*b*, 1995, 1996, 1997). The underlying attractiveness of beginning with the integral form is that the reflective boundary conditions arise simply and explicitly as part of the coupled equations, and that well known and physically appealing Green's function/diagrammatic techniques can be employed for numerical solution. Indeed, it is through an appropriate choice of an evanescent Green's function that Dudarev & Whelan (1994*a*,*b*) obtained their closed-form solution to the specular reflection coefficient of platinum(111) and, further, that this has also been reproduced by us using well known diagrammatic techniques (Derlet & Smith, 1997). Additional work by Dudarev & Whelan has demonstrated that the total real-space density of states derived from the imaginary part of the Green's function can shed much light on the origin of (say) the surface resonance problem (Dudarev & Whelan, 1997).

In the present work, we consider the numerical solution to the reflection problem in the coupled integral equation form using Green's-function techniques. In particular, we demonstrate from first principles an iterative numerical scheme to calculate the reflection coefficient for the '*n*-rod' scattering problem. Then, in a natural extension to this, we enumerate the finite number of diagrammatic contributions to the local real-space Green's function, leading again to a numerically stable procedure for its evaluation. It is from this that the local and total density of states can be obtained for any material considered. We conclude *via* preliminary application of these numerical schema to platinum(111) for comparison with recent analytical work.

† Now at Department of Physics, Norwegian University of Science and Technology, N-7034 Trondheim, Norway.

ISSN 0108-7673

2. The geometry of the surface and the problem of convergence

The free three-dimensional approximately relativistic Schrödinger Green's function for an electron (Wang, 1995) is given by

$$G(\mathbf{r}, \mathbf{r}'; E) = -\frac{m}{2\pi\hbar^2}\frac{\exp(ik|\mathbf{r}-\mathbf{r}'|)}{|\mathbf{r}-\mathbf{r}'|}, \tag{1}$$

where $k = (2mE\gamma/\hbar^2)^{1/2}$. Here, γ is the Lorentz boost factor. Equation (1) has the virtue of decaying inversely as a function of the distance between two locations in space and it is through this property that we can intuitively connect with the notion that, in interacting with the surface, the electron does not penetrate significantly into the solid.

However, by exploiting the two-dimensional periodicity of the surface scattering problem, we employ the two-dimensional Fourier transform (parallel to the surface) of (1):

$$G(z, z'; E, \mathbf{k}_\parallel) = -\frac{im}{\hbar^2 k_z}\exp(ik_z|z-z'|), \tag{2}$$

where $k_z = (2m\gamma E/\hbar^2 - \mathbf{k}_\parallel^2)^{1/2}$. Unlike (1), (2) no longer has the virtue of decaying inversely as $|z-z'|$ for real k_z and any multiple-scattering perturbation expansion now begins with a plane-wave basis with respect to the direction perpendicular to the surface. Physically, this simply arises from delocalization of the electron parallel to the surface, thereby immediately destroying through coherent interference of (1) (effectively a Huygens's principle) the local nature of the electron's interaction with the surface. For a particular choice of $\mathbf{k}_\parallel$ and E, k_z can become imaginary and nonpropagating solutions can also arise in the direction of z. These are evanescent modes and, within this regime, the corresponding Green's function will be referred to as an evanescent Green's function.

The obvious advantage of this prescription is that the mathematical problem is considerably simplified with the reduction from three degrees of spatial freedom to one. However, through such a choice of 'basis', one must now include multiple scattering deep within the solid to obtain well converged reflection coefficients since processes that intuitively occur at or near the surface region now depend on the one-dimensional semi-bulk electronic eigenstates admitted by (2) and the corresponding one-dimensional crystal potential.

3. Formal Green's-function theory

For a plane-wave electron incident on a semi-infinite crystal with wavevector $\mathbf{k} = (\mathbf{k}_\parallel, k_z)$, the Schrödinger equation can be written as a series of coupled one-dimensional equations (Wang, 1995, p. 68):

$$-\frac{\hbar^2}{2m}\frac{d^2}{dz^2}\varphi_{\mathbf{k}_\parallel-\mathbf{g}_\parallel}(z) + \sum_{\mathbf{g}'_\parallel} U_{\mathbf{g}_\parallel-\mathbf{g}'_\parallel}(z)\varphi_{\mathbf{k}_\parallel-\mathbf{g}'_\parallel}(z) = (\hbar^2 k^2_{\mathbf{g}_\parallel}/2m)\varphi_{\mathbf{k}_\parallel-\mathbf{g}_\parallel}(z), \tag{3}$$

in which $U_{\mathbf{k}_\parallel-\mathbf{g}_\parallel}(z)$ and $\varphi_{\mathbf{g}_\parallel}(z)$ are the two-dimensional Fourier transforms of the three-dimensional crystal potential $U(\mathbf{r})$ and the electronic wave-function solution $\varphi_{\mathbf{k}}(\mathbf{r})$. The $\mathbf{g}_\parallel$ constitute the two-dimensional reciprocal-lattice vectors parallel to the crystal surface and $k^2_{\mathbf{g}_\parallel} = k^2 - (\mathbf{k}_\parallel + \mathbf{g}_\parallel)^2$, where $\hbar^2 k^2_{\mathbf{g}_\parallel}/2m$ is the energy associated with the electron motion normal to the surface. For notational brevity, we now assume all vectors to be two dimensional and parallel to the surface, and also shift the reciprocal-space origin to $\mathbf{k}_\parallel$. In this notation, (3) becomes

$$-\frac{\hbar^2}{2m}\frac{d^2}{dz^2}\varphi_{\mathbf{g}}(z) + \sum_{\mathbf{g}'} U_{\mathbf{g}-\mathbf{g}'}(z)\varphi_{\mathbf{g}'}(z) = (\hbar^2 k^2_{\mathbf{g}_\parallel}/2m)\varphi_{\mathbf{g}}(z). \tag{4}$$

The corresponding integral equations for the $\varphi_{\mathbf{g}}(z)$ are then given by

$$\varphi_{\mathbf{g}}(z) = \varphi^{(0)}_{\mathbf{g}}(z) + \sum_{\mathbf{g}'}\int \mathrm{d}z' G^{(0)}_{\mathbf{g}}(z, z')U_{\mathbf{g}-\mathbf{g}'}(z')\varphi_{\mathbf{g}'}(z'), \tag{5}$$

where $\varphi^{(0)}_{\mathbf{g}}(z)$ is the homogeneous solution and $G^{(0)}_{\mathbf{g}}(z, z')$ the corresponding homogeneous Green's function. For the reflection problem, we consider a wave incident onto the semi-infinite medium, facilitating the (zeroth-order) homogeneous solution as $\varphi^{(0)}_{\mathbf{g}}(z) = \exp(ik_0 z)\delta_{\mathbf{g},0}$, and the zeroth-order one-dimensional Green's function, (2), as $G^{(0)}_{\mathbf{g}}(z, z') = im/\hbar^2 k_{\mathbf{g}}\exp(ik_{\mathbf{g}}|z-z'|)$.

The exact Green's functions also satisfy a series of integral equations with respect to the $G^{(0)}_{\mathbf{g}}(z, z')$:

$$G_{\mathbf{g}\mathbf{g}'}(z, z') = G^{(0)}_{\mathbf{g}}(z, z')\delta_{\mathbf{g},\mathbf{g}'} + \sum_{\bar{\mathbf{g}}}\int \mathrm{d}\bar{z}\, G^{(0)}_{\mathbf{g}}(z, \bar{z})U_{\mathbf{g}-\bar{\mathbf{g}}}(\bar{z}) \times G_{\bar{\mathbf{g}}\mathbf{g}'}(\bar{z}, z'). \tag{6}$$

Here we note the resulting exact Green's function is no longer diagonal with respect to momentum; that is, the crystal potential induces transitions between different momenta admitted by the two-dimensional crystal geometry.

3.1. *The solution to an infinitesimally thin slab*

To investigate the solution of (6), we first consider only the specular case. That is we ignore all $\mathbf{g}$ modes apart from $\mathbf{g} = 0$; the so-called single-rod approximation. Equation (6) thus simplifies to

$$G_0(z, z') = G^{(0)}_0(z, z') + \int \mathrm{d}\bar{z}\, G^{(0)}_0(z, \bar{z})U_0(\bar{z})G_0(\bar{z}, z'), \tag{7}$$

constituting an electron in the one-dimensional laterally averaged crystal potential. An analytic solution to this

simplified integral equation is equally intractable without further approximation.

Insight can nevertheless be gained by investigating the solution for a single slab of width d, centered at z_0. The integral equation then becomes

$$G_0(z, z') = G_0^{(0)}(z, z') + \int_{z_0-d/2}^{z_0+d/2} \mathrm{d}\overline{z}\, G_0^{(0)}(z, \overline{z}) U_0(\overline{z}) G_0(\overline{z}, z'). \tag{8}$$

If $d \ll 2\pi/k_0$, then to a first approximation we have

$$G_0(z, z') = G_0^{(0)}(z, z') + dG_0^{(0)}(z, z_0) U_0(z_0) G_0(z_0, z'), \tag{9}$$

which upon iteration becomes

$$\begin{aligned} G_0(z, z') &= G_0^{(0)}(z, z') + dG_0^{(0)}(z, z_0) U_0(z_0) \\ &\quad \times \{1 + dU_0(z_0) G_0^{(0)}(z_0, z_0) \\ &\quad + [dU_0(z_0) G_0^{(0)}(z_0, z_0)]^2 + \ldots\} G_0^{(0)}(z_0, z') \\ &= G_0^{(0)}(z, z') + G_0^{(0)}(z, z_0) \\ &\quad \times \frac{dU_0(z_0)}{1 - dU_0(z_0) G_0^{(0)}(z, z_0)} G_0^{(0)}(z_0, z'). \end{aligned} \tag{10}$$

Substitution of (2) into the above then gives

$$g_0(z, z') = g_0^{(0)}(z, z') + g_0^{(0)}(z, z_0) \frac{\alpha_0(z_0)}{1 - \alpha_0(z_0)} g_0^{(0)}(z_0, z'), \tag{11}$$

where we have used the notation

$$g_0(z, z') = (im/\hbar^2 k_0)^{-1} G_0(z, z'), \tag{12}$$

$$g_0^{(0)}(z, z') = \exp(ik_0|z - z'|), \tag{13}$$

and

$$\alpha_0(z) = imdU_0(z)/\hbar^2 k_0. \tag{14}$$

Both the reflection and transmission coefficient for the thin slab at z_0 can be determined directly from (11) by suitable choice of z and z'. For example, with $z = z' < z_0$ and using (13), (11) reduces to

$$g_0(z, z) = 1 + \exp[-i2k_0(z - z_0)] \frac{\alpha_0(z_0)}{1 - \alpha_0(z_0)}. \tag{15}$$

The first term represents the 'self-scattering' at z due to the (zeroth-order) homogeneous solution, and the second term represents the contribution due to propagation from z to z_0, reflection at z_0, and propagation back to z. Thus, by inspection, the reflection coefficient must equal $\alpha_0(z_0)/[1 - \alpha_0(z_0)]$. In a similar way, the transmission coefficient can be found (by choosing $z < z_0 < z'$) to equal $1/[1 - \alpha_0(z_0)]$. It is important to note that (11) constitutes the *exact* solution to (9) for a thin slab satisfying $d \ll 2\pi/k_0$ and that, regardless of the strength of the scatterer, the magnitude of the sum of the reflection and transmission coefficients will always be less than (we anticipate absorption) or equal to unity.

The generalization of (11) to the n-rod case then simply becomes the generalization to an equivalent matrix equation:

$$\begin{aligned} \tilde{g}(z, z') &= \tilde{g}^{(0)}(z, z_0) + \tilde{g}^{(0)}(z, z_0) \tilde{\alpha}(z_0) [\tilde{I} - \tilde{\alpha}(z_0)]^{-1} \\ &\quad \times \tilde{g}^{(0)}(z_0, z'), \end{aligned} \tag{16}$$

where

$$[\tilde{g}^{(0)}(z, z')]_{\mathbf{g}\mathbf{g}'} = \exp(ik_{\mathbf{g}}|z - z'|)\delta_{\mathbf{g},\mathbf{g}'} \tag{17}$$

and

$$[\tilde{\alpha}(z)]_{\mathbf{g}\mathbf{g}'} = imdU_{\mathbf{g}-\mathbf{g}'}(z)/\hbar^2 k_{\mathbf{g}}. \tag{18}$$

In analogy with the specular case, the resulting reflection matrix is given by

$$\tilde{r}(z_0) = \tilde{\alpha}(z_0)[\tilde{I} - \tilde{\alpha}(z_0)]^{-1} \tag{19}$$

and the transmission matrix as

$$\tilde{t}(z_0) = [\tilde{I} - \tilde{\alpha}(z_0)]^{-1}. \tag{20}$$

Here the off-diagonal terms represent the exact amplitudes for reflection scattering, (19), or transmission scattering, (20), between modes within the infinitesimal slab.

3.2. *The reflection matrix for a general potential*

To obtain the reflection coefficient for the full crystal potential, we break the (Fourier-transformed parallel to the surface) potential into thin slabs of thickness d in which the approximation entailed in (9) remains valid. Consider two such neighboring slabs at z_0 and z_1. Equations (19) and (20) allow the immediate determination of the individual reflection and transmission matrices for each slab, giving $\tilde{r}_0$, $\tilde{t}_0$, $\tilde{r}_1$ and $\tilde{t}_1$.

The reflection matrix when approaching from the left can then be written down trivially by a Green's function expansion. That is,

$$\begin{aligned} \tilde{R}^l &= \tilde{r}_0 + \tilde{t}_0 \tilde{g}(z_0, z_1) \tilde{r}_1 \tilde{g}(z_1, z_0) \tilde{t}_0 \\ &\quad + \tilde{t}_0 \tilde{g}(z_0, z_1) \tilde{r}_1 \tilde{g}(z_1, z_0) \tilde{r}_0 \tilde{g}(z_0, z_1) \tilde{r}_1 \tilde{g}(z_1, z_0) \tilde{t}_0 + \ldots. \end{aligned} \tag{21}$$

Here the first term represents a direct (bare) reflection from the first slab, whereas the second term represents the reflection contribution by first transmission through z_0, propagation to z_1, reflection at z_1, propagation back to z_0 and transmission at z_0. Higher-order contributions involve internal reflections between z_0 and z_1, and can be represented *via* a simple geometrical series giving the final closed-form solution as

$$\tilde{R}^l = \tilde{r}_0 + \tilde{t}_0 \tilde{e} \tilde{r}_1 \tilde{e} (\tilde{I} - \tilde{r}_0 \tilde{e} \tilde{r}_1 \tilde{e})^{-1} \tilde{t}_0. \tag{22}$$

Here we have used

$$\tilde{e} = \tilde{g}(z_0, z_1) = \tilde{g}(z_1, z_0), \tag{23}$$

which represents free propagation between z_0 and z_1. Similar derivations exist for R^r, the reflection matrix when approaching from the right, and T^l and T^r, the corresponding transmission matrices.

If we now consider an array of three slabs, each separated by a distance d, then the reflection and transmission matrices can easily be written by iterating the above formalism. It becomes simply a matter of calculating the total reflection and transmission matrices of the first two slabs, and then applying the same method to the composite system (consisting of the first two slabs) and a third slab. This procedure can be iterated for any number of slabs to calculate the reflection and transmission matrices for an arbitrary potential. The complete recurrence relations for the nth composite system consisting of n slabs, a distance d apart, are found to be

$$\tilde{R}_n^l = \tilde{R}_{n-1}^l + \tilde{T}_{n-1}^r \tilde{e}\tilde{r}_n\tilde{e}(\tilde{I} - \tilde{R}_{n-1}\tilde{e}\tilde{r}_n\tilde{e})^{-1}\tilde{T}_{n-1}^l \tag{24}$$

$$\tilde{T}_n^l = \tilde{t}_n\tilde{e}(\tilde{I} - \tilde{R}_{n-1}\tilde{e}\tilde{r}_n\tilde{e})^{-1}\tilde{T}_{n-1}^l \tag{25}$$

$$\tilde{R}_n^r = \tilde{r}_n + \tilde{t}_n\tilde{e}\tilde{R}_{n-1}^r\tilde{e}(\tilde{I} - \tilde{r}_n\tilde{e}\tilde{R}_{n-1}^r\tilde{e})^{-1}\tilde{t}_n \tag{26}$$

$$\tilde{T}_n^r = \tilde{T}_{n-1}\tilde{e}(\tilde{I} - \tilde{r}_n\tilde{e}\tilde{R}_{n-1}^r\tilde{e})^{-1}\tilde{t}_n, \tag{27}$$

where $\tilde{r}_n$ and $\tilde{t}_n$ are the reflection and transmission matrices due to only the nth slab and $R_n^{r(l)}$ and $T_n^{r(l)}$ are the right (left) reflection and transmission matrices for the composite system of n slabs.

3.3. *The real-space local density of states*

The three-dimensional Green's function $G(\mathbf{r}, \mathbf{r}; E)$ represents the amplitude due to the particle's self-scattering at $\mathbf{r}$ and, when Fourier transformed into the time domain, represents the amplitude connecting an electron at $\mathbf{r}$ at time $t = 0$, and an electron at $\mathbf{r}$ at a time t later. Thus, in the energy domain, $G(\mathbf{r}, \mathbf{r}; E)$ represents the amplitude of an electron at $\mathbf{r}$ with energy E. It is easily shown (Economou, 1983) that the imaginary part of this quantity in turn gives the density of available states at $\mathbf{r}$:

$$\rho(\mathbf{r}; E) = -2\pi\Im[G(\mathbf{r}, \mathbf{r}; E)]. \tag{28}$$

For a free electron, the onsite three-dimensional Green's function, (1), gives the local density of states (DOS) as

$$\rho(\mathbf{r}; E) = mk/\hbar^2, \tag{29}$$

which can be easily verified by the more familiar $\rho(\mathbf{r}; E) = \rho(E) = \int \mathrm{d}^3\mathbf{q}\,\delta(E - E_{\mathbf{q}})/4\pi$.

In an analogous manner, the imaginary part of the one-dimensional (Fourier transformed parallel to the surface) Green's function is proportional to the density of available states for an electron with two-dimensional wavevector $\mathbf{k}_\parallel$ at z. That is,

$$\rho(z; E, \mathbf{k}_\parallel) = -2\pi\Im[G(z, z; E, \mathbf{k}_\parallel)] = m/\hbar^2 k_z, \tag{30}$$

where $k_z = (2m\gamma E/\hbar^2 - \mathbf{k}_\parallel^2)^{1/2}$. This can again be derived *via* $\rho(z; E) = \rho(E) = \int \mathrm{d}q_z\,\delta(E - E_{\mathbf{q}_z})$. For the case of an electron in a crystal potential, the DOS is given by

$$\rho(z; E) = -2\pi\,\mathrm{Trace}\{\Im[\tilde{G}(z, z; E)]\} \tag{31}$$

$$= -2\pi\sum_{\mathbf{q}}\Im[G_{\mathbf{qq}}(z, z; E)], \tag{32}$$

where $G_{\mathbf{qq}}$ is defined *via* (6). Here, the local DOS arises as contributions from each allowed scattering mode $\mathbf{q}$. We refer to each of these individual contributions as $\rho_{\mathbf{q}}(z; E)$ $(= -2\pi\Im[G_{\mathbf{qq}}(z, z; E)])$, giving

$$\rho(z; E) = \sum_{\mathbf{q}}\rho_{\mathbf{q}}(z; E). \tag{33}$$

The total, in the sense of the direction perpendicular to the surface, electronic DOS is given as the z-space integral of the local density of states, *i.e.*

$$\rho_{\mathbf{q}}(E) = \lim_{L\to\infty}(1/L)\int_{L/2}^{-L/2}\mathrm{d}z\,\rho_{\mathbf{q}}(z; E)$$

$$= -2\pi\Im\left[\lim_{L\to\infty}(1/L)\int_{L/2}^{-L/2}\mathrm{d}z\,G_{\mathbf{qq}}(z, z; E)\right], \tag{34}$$

where again $\rho(E) = \sum_{\mathbf{q}}\rho_{\mathbf{q}}(E)$ which constitutes the traditional DOS encountered in solid-state physics. For a semi-infinite material system, the integral breaks down to an integral over the local Green's functions:

$$(1/L)\int_{-L/2}^{0}\mathrm{d}z\,G^l(z, z; E) + (1/L)\int_{0}^{L/2}\mathrm{d}z\,G^r(z, z; E). \tag{35}$$

Here $G^l(z, z; E)$ is the exact Green's function outside the semi-infinite material and by inspection of (15) will have the generic form

$$\frac{im}{\hbar^2 k}[1 + \exp(i2kz)R], \tag{36}$$

where R is the reflection coefficient/matrix of the material beginning at $z = 0$. In (35), $G^r(z; E)$ is the exact Green's function within the solid. Equation (35) thus reduces to

$$\tfrac{1}{2}\left[\frac{im}{\hbar^2 k} + \frac{2}{L}\int_0^{L/2}\mathrm{d}z\,G^r(z, z; E)\right] \tag{37}$$

where the second term within the brackets is expected to converge to a finite value for large $L/2$.

Inspection of the DOS derived from the free one-dimensional electronic Green's function, (30), indicates that the effect of a crystal potential will be largely 'drowned out' for small k_z owing to its dependence on the inverse of k_z: an artifact of the 'particle in the box' normalization conditions. For the present work, we

investigate the more physically transparent relative DOS, which we define as

$$\overline{\rho}_{\mathbf{q}}(z; E) = \frac{\rho_{\mathbf{q}}(z; E)}{2\pi |G^{(0)}_{\mathbf{q}}(z, z; E)|}. \tag{38}$$

4. Local density of states for an arbitrary potential

To obtain the real-space onsite Green's-function matrix at the slab (say) z_0 within a solid, we consider the system described in Fig. 1. Here the slab of interest, at z_0, forms part of an array of crystal potential slabs each defined by a transmission and reflection coefficient. Again all are separated by a distance d. Since we require the self-scattering amplitude for z_0, only the composite reflection matrix from the left, starting at z_l, and the composite reflection matrix from the right, starting at z_r, are needed. These are assumed to have been calculated using the iterative scheme detailed in the last section and are referred to as $\tilde{R}_l$ and $\tilde{R}_r$.

With respect to the free one-dimensional Green's function, the relevant scattering components arising from Fig. 1 (the slab at z_0, $\tilde{R}_l$ and $\tilde{R}_r$) are displayed in Fig. 2(a). The contribution to the local Green's function due *only* to the slab at z_0 can be accounted for exactly using (16), suggesting that in calculating the full onsite Green's function, $\tilde{g}(z_0, z_0)$, we use (16) [the solution to the n-rod generalization of (7)] as the homogeneous solution rather than (2).

Thus, with respect to (16), there will exist no explicit scattering at z_0 and only scattering with, and between, the left and right reflection matrices: $\tilde{R}_l$ and $\tilde{R}_r$. The use of (16) as the homogeneous solution also admits additional self-scattering at z_l and z_r, thus renormalizing both the left and right composite reflection matrix. That is,

$$\tilde{R}'_r = \{\tilde{I} - \tilde{R}_r[\tilde{g}^{(1)}(z_r, z_r) - \tilde{I}]\}^{-1}\tilde{R}_r \tag{39}$$

$$\tilde{R}'_l = \{\tilde{I} - \tilde{R}_l[\tilde{g}^{(1)}(z_l, z_l) - \tilde{I}]\}^{-1}\tilde{R}_l. \tag{40}$$

Here, in both denominators, we have subtracted off the self-scattering due to the free Green's function $[g^{(0)}(z_l, z_l) = g^{(0)}(z_r, z_r) = 1]$ since this has already been accounted for in the calculation of $\tilde{R}_r$ and $\tilde{R}_l$. It must always be remembered that the reflection and transmission quantities of a slab do not represent bare potential scattering but rather an already renormalized scattering due to potential self-scattering. The new relevant scattering components ($\tilde{R}'_l$ and $\tilde{R}'_r$) are shown in Fig. 2(b), where the central slab is no longer explicitly included. Fig. 3 reveals that there exists a small finite number of unique diagram topologies arising from scattering between the renormalized right and left reflection matrices. The diagrammatic elements follow the usual conventions in that lines represent particle propagation and dots represent scattering (Economou, 1983, ch. 7). In this case, however, the dots represent an arbitrary slab representation of the crystal potential rather than distinctly (physical) atomic planes such as in our previous work (Derlet & Smith, 1997). The larger dots represent all possible self-scattering at a slab due to

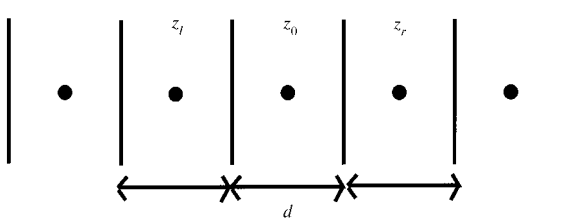

Fig. 1. To calculate the local real-space Green's function at z_0, we must consider the system consisting of the (slab) potential at z_0, all reflection/transmission matrices to the left (beginning at z_l), and all reflection/transmission matrices to the right (beginning at z_r).

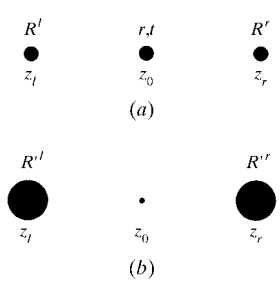

Fig. 2. The scattering components (a) with respect to the free Green's function, and (b) with respect to the exact Green's function for the central slab. In the latter, diagrammatically, there exists no scattering at z_0 and the corresponding left and right reflection matrices are now also renormalized to include the additional self-scattering arising from (16) being the homogeneous solution.

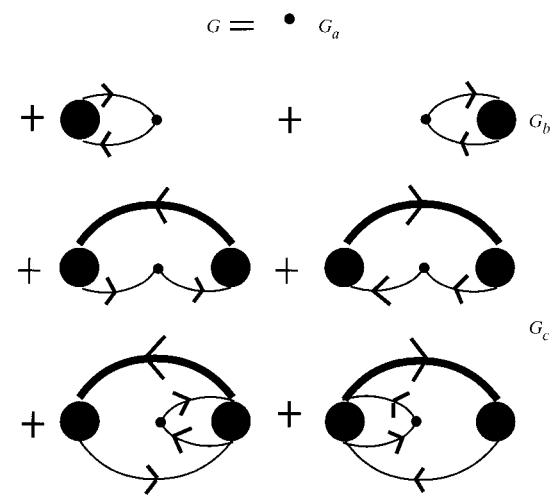

Fig. 3. Diagrammatic expansion of real-space on-slab Green's function with respect to the scattering components in Fig. 2(b). The propagating line represents the exact Green's function for the central slab displayed in Fig. 2(a). The thickened line represents the renormalized propagation taking into account all internal reflections between z_l and z_r.

the use of (16) as the homogeneous solution, and the thick lines represent internal scattering between the end-points of the propagating line.

With these objects in mind, we can now easily write down all contributions to the full onsite Green's function, again, *via* a simple geometric series expansion. From Fig. 3, the contribution due only to the single slab has already been taken into account *via* the exact Green's function for the slab at z_0. Thus, the lowest-order contribution is simply:

$$\tilde{G}_a = \tilde{g}^{(1)}(z_0, z_0). \tag{41}$$

The next-order contributions arise from two terms, each taking into account scattering between z_0 and the reflection matrices at z_l and z_r, giving

$$\tilde{G}_b = \tilde{g}^{(1)}(z_0, z_l)\tilde{R}'_l\tilde{g}^{(0)}(z_l, z_0) + \tilde{g}^{(1)}(z_0, z_r)\tilde{R}'_r\tilde{g}^{(1)}(z_r, z_0). \tag{42}$$

Note that multiple scattering between z_0 and z_l (or z_r) can be explicitly revealed by substitution of (39) and (40) into (42), and the use of (16) for $\tilde{g}^{(1)}(z, z')$.

All remaining contributions are included in the last four diagrams. These 'second-order' contributions arise from a class of diagrams involving additional scattering between $\tilde{R}'_l$ and $\tilde{R}'_r$ in which the first scatter is with $\tilde{R}'_r$ ($\tilde{R}'_l$) and the last with $\tilde{R}'_l$ ($\tilde{R}'_r$). Also included are those contributions in which the first and last scatters occur at $\tilde{R}'_r$ or $\tilde{R}'_l$. These contributions to the Green's function can also be easily written as:

$$\begin{aligned}
\tilde{G}_c = {} & \tilde{g}^{(1)}(z_0, z_l)[\tilde{I} - \tilde{R}'_l\tilde{g}^{(1)}(z_l, z_r)\tilde{R}'_r\tilde{g}^{(1)}(z_r, z_l)]^{-1} \\
& \times \tilde{R}'_l\tilde{g}^{(1)}(z_l, z_r)\tilde{R}'_r\tilde{g}^{(1)}(z_r, z_0) \\
& + \tilde{g}^{(1)}(z_0, z_r)[\tilde{I} - \tilde{R}'_r\tilde{g}^{(1)}(z_r, z_l)\tilde{R}'_l\tilde{g}^{(1)}(z_l, z_r)]^{-1} \\
& \times \tilde{R}'_r\tilde{g}^{(1)}(z_r, z_l)\tilde{R}'_l\tilde{g}^{(1)}(z_l, z_0) \\
& + \tilde{g}^{(1)}(z_0, z_r)\tilde{R}'_r\tilde{g}^{(1)}(z_r, z_l)\tilde{R}'_l\tilde{g}^{(1)}(z_l, z_r) \\
& \times [\tilde{I} - \tilde{R}'_r\tilde{g}^{(1)}(z_r, z_l)\tilde{R}'_l\tilde{g}^{(1)}(z_l, z_r)]^{-1}\tilde{R}'_r\tilde{g}^{(1)}(z_r, z_0) \\
& + \tilde{g}^{(1)}(z_0, z_l)\tilde{R}'_l\tilde{g}^{(1)}(z_l, z_r)\tilde{R}'_r\tilde{g}^{(1)}(z_r, z_l) \\
& \times [\tilde{I} - \tilde{R}'_l\tilde{g}^{(1)}(z_l, z_r)\tilde{R}'_r\tilde{g}^{(1)}(z_r, z_l)]^{-1}\tilde{R}'_l\tilde{g}^{(1)}(z_l, z_0).
\end{aligned} \tag{43}$$

Hence we have $\tilde{g}(z_0, z_0) = \tilde{G}_a + \tilde{G}_b + \tilde{G}_c$ and the exact Green's function is then given by

$$\tilde{G}(z_0, z_0) = \mathrm{Diag}\left[\left(\frac{im}{\hbar^2 k_{\mathbf{g}_0}}\right), \left(\frac{im}{\hbar^2 k_{\mathbf{g}_1}}\right), \ldots\right]\tilde{g}(z_0, z_0), \tag{44}$$

from which the local and total DOS can be obtained using (32).

5. Platinum(111)

The (111) surface of platinum has been of interest as a test-bed for recent analytical studies of corresponding surface resonance modes within RHEED (Dudarev & Whelan, 1994*a*,*b*, 1995, 1996; Derlet & Smith, 1997). As part of this work, Dudarev & Whelan (1994*a*,*b*, 1995, 1996) have determined a more realistic (Doyle–Turner-type) description of the real and imaginary crystal potential of bulk platinum, which, owing to the lack of significant surface reconstruction, can be used to construct a potential for the ideal (111) cleave. As with theirs and our previous work, we consider the RHEED intensity profile due to incident 100 keV electrons for a range of low glancing angles and azimuthal angles, the zero of which is in the $[1\bar{2}0]$ direction. In all of the following numerical results, convergence to the semi-bulk limit was obtained by using up to 80 atomic planes, each separated into 140 slabs. This choice satisfies the $d \ll 2\pi/k_0$ requirement for the thin-slab approximation.

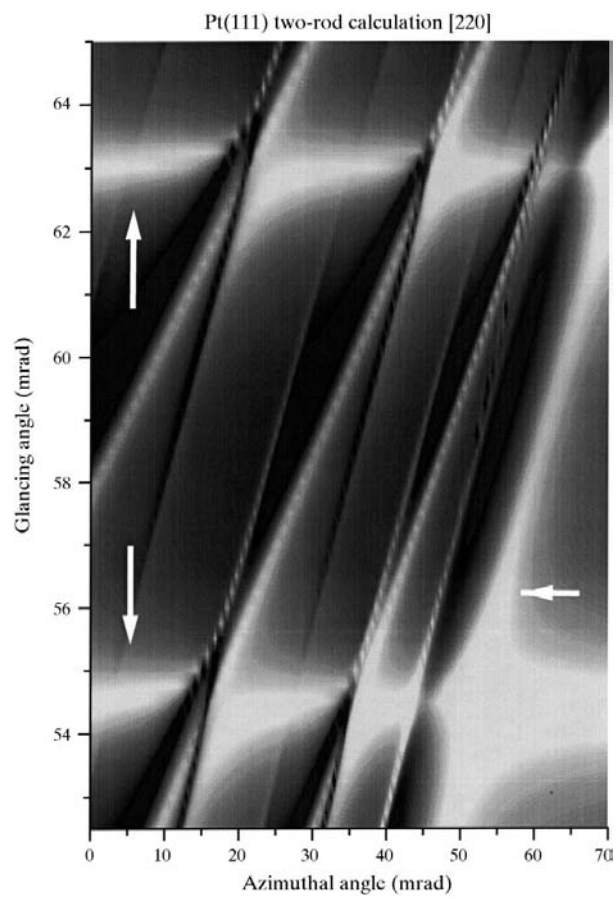

Fig. 4. RHEED intensity profile for specular beam. The two vertical white arrows indicate two horizontal Kikuchi lines, whilst the horizontal arrow points to the resonance parabola. Elements of the Kikuchi envelope are also evident. The rippled effect is due to smoothing over a data set with a resolution far less than that of the picture. Image over-exposed to display all finer detail.

Fig. 4 represents the resulting specular intensity spectra arising from a two-rod calculation in which scattering between $\mathbf{g}_0 = 0$ and $\mathbf{g}_0 = (\bar{2}20)$ is considered. The distinctive horizontal lines due to 777 and 888 Bragg elastic reflections can clearly be seen, as well as the surface resonance parabolae studied by Dudarev & Whelan. These lines are often referred to as Kossel lines; however, in the present work, we refer to them as horizontal Kikuchi lines to be consistent with previous recent work (Dudarev & Whelan, 1994*a*,*b*, 1995, 1996; Derlet & Smith, 1997). This terminology has its origins in that inelastic thermal diffuse scattering within RHEED is equivalent to large-angle convergent-beam diffraction and hence similar to simply rocking the incident electron beam. In Fig. 4, tangent lines to the left of the resonance parabola, constituting the so-called Kikuchi envelope, are also clearly evident.

Figs. 5 and 6 display the reflection coefficients for two incident glancing angles. These are respectively 58.6 mrad, which occurs midway between the 777 and 888 Bragg reflections (at the so-called off-Bragg reflection condition), and 54.6 mrad corresponding to the 777 Bragg reflection condition. For both figures, in addition to the specular case, the reflection coefficient of the $(\bar{2}20)$ side beam is also displayed as a function of incident *azimuthal* angle. Also marked in both figures is the emergence angle for the $(\bar{2}20)$ beam. For incident azimuthal angles greater than this, the $(\bar{2}20)$ beam no longer emerges, constituting an evanescent wave propagating in a direction parallel to the surface. The large right-most peak in the specular reflection coefficient, occurring at an azimuthal angle of ~ 60.7 mrad in Fig. 5 and ~ 52.0 mrad in Fig. 6, corresponds to the surface-resonance mode identified and studied by Dudarev & Whelan.

Fig. 7 represents the $(\bar{2}20)$ local relative DOS, (38), (at a glancing angle of 58.6 mrad), evaluated at the (111) surface atomic layer using both the one- and two-rod approximations. We note that the local relative DOS derived from the free $(\bar{2}20)$ Green's function would entail a step function at the emergence angle of the $(\bar{2}20)$ side beam; in this case, an azimuthal angle of approximately 51 mrad. Inspection of the surface-resonance feature indicates that (at least) a two-rod approximation

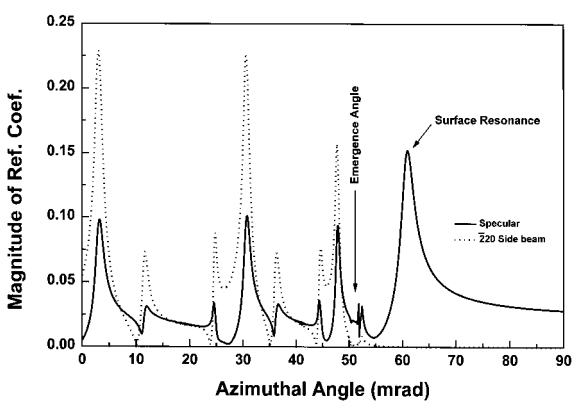

Fig. 5. Specular and $(\bar{2}20)$ side-beam reflection coefficient for a glancing angle of 58.6 mrad (off-Bragg condition).

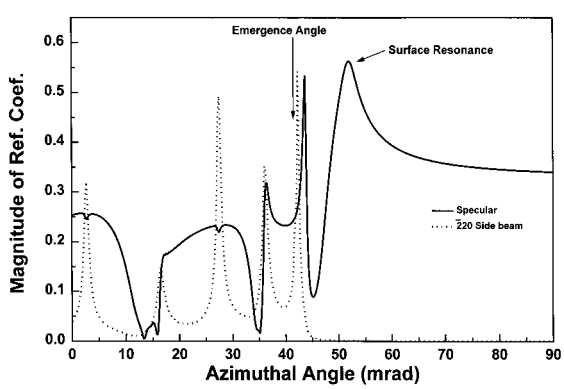

Fig. 6. Specular and $(\bar{2}20)$ side-beam reflection coefficient for a glancing angle of 54.6 mrad (Bragg condition).

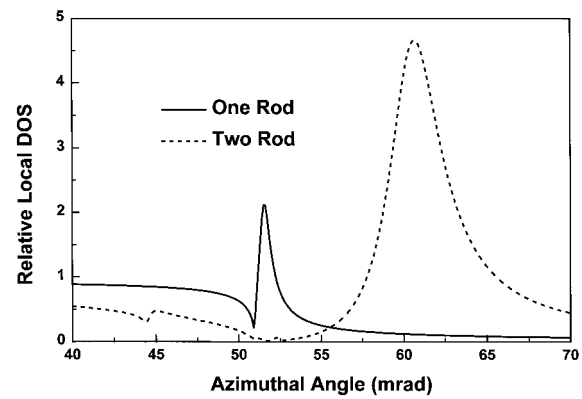

Fig. 7. The local relative DOS evaluated at the outermost atomic layer calculated using both one- and two-rod approximations. Glancing angle: 58.6 mrad (off-Bragg condition).

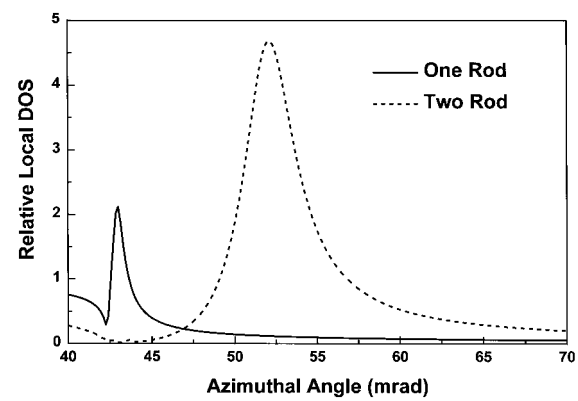

Fig. 8. The local relative DOS evaluated at the outermost atomic layer calculated using both a one- and a two-rod approximation. Glancing angle: 54.6 mrad (Bragg condition).

is required to adequately reproduce the Green's-function pole structure responsible for the surface resonance mode. A similar calculation is displayed in Fig. 8 for the 777 specular Bragg reflection condition (a glancing angle of 54.6 mrad). Its similarities with Fig. 7 suggest that the distribution of $(\bar{2}20)$ scattering-mode states is largely independent of Bragg/off-Bragg (coherent/incoherent) multiple scattering of the specular mode.

To investigate the spatial distribution [over the first four Pt (111) planes] of electronic states that contribute to the surface resonance mode, we calculate as an example the local relative DOS for the $\mathbf{g}_0 = (\bar{2}20)$ scattering mode within the one- and two-rod approximations. For both the one- and two-rod calculations, we choose the azimuthal angle of the incident electron as that angle corresponding to the peak of the surface-resonance mode determined from Fig. 7 for the off-Bragg scattering condition and from Fig. 8 for the Bragg scattering condition.

In Fig. 9, we first consider the off-Bragg glancing angle 58.6 mrad. For the single-rod calculation, Fig. 9 displays the relative local DOS evaluated for the incident azimuthal angle of ~ 51.6 mrad, and in the case of the two-rod calculation an incident azimuthal angle of ~ 60.7 mrad. In both cases, we see that the $(\bar{2}20)$ contribution is well localized at the (111) atomic layers and, in the case of the one-rod calculation, a twin peak structure exists. In the two-rod calculation, this feature is lost and the peaks significantly broaden due to the interplane scattering *via* the specular mode. Fig. 10 repeats the calculation (for appropriate incident azimuthal angles derived from Fig. 8) for the Bragg glancing angle of 54.6 mrad and again we observe that the distribution of states is unaffected by coherent/incoherent specular scattering. In both Figs. 9 and 10, the relative local DOS remains similar for each atomic layer and it is found that this feature extends throughout the semi-infinite solid.

Figs. 11(*a*) and (*b*) represent the total relative DOS, (34), for the specular and $(\bar{2}20)$ scattering modes, for the two glancing-angle geometries presently considered: 58.8 and 54.6 mrad. We remind the reader that the total specular relative DOS derived from the equivalent free-space Green's function would be a constant equal to unity, and for the $(\bar{2}20)$ mode would be a step function at an azimuthal angle of ~ 51 mrad for (*a*) and ~ 40 mrad

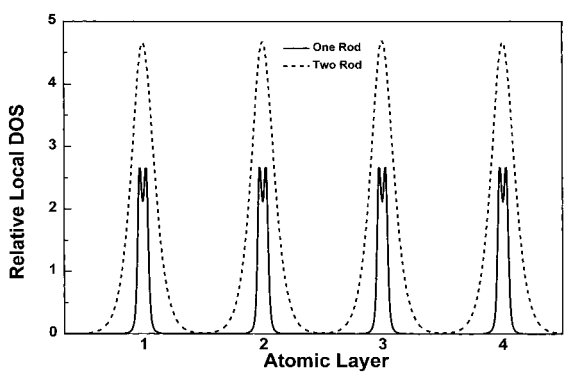

Fig. 9. The $(\bar{2}20)$ mode real-space local relative DOS calculated using both one- and two-rod approximations. Glancing angle of 58.6 mrad (off-Bragg scattering condition).

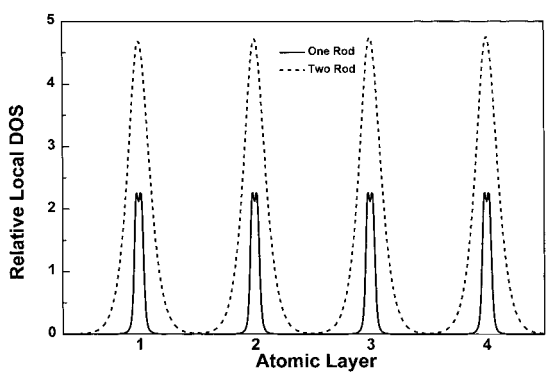

Fig. 10. The $(\bar{2}20)$ mode real-space local relative DOS calculated using both one- and two-rod approximations. Glancing angle of 54.6 mrad (off-Bragg scattering condition).

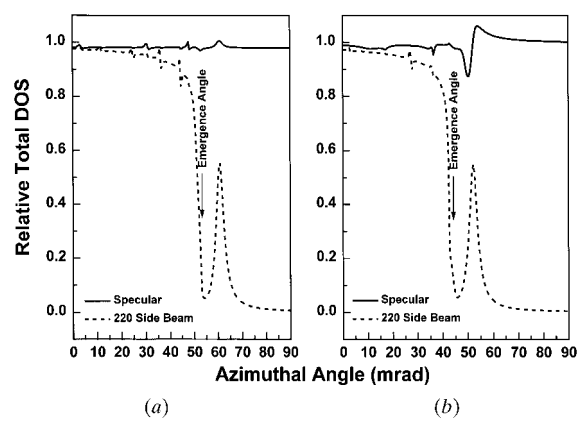

(*a*) (*b*)

Fig. 11. The specular and $(\bar{2}20)$ side beam total relative DOS for glancing angles (*a*) 58.6 mrad and (*b*) 54.6 mrad.

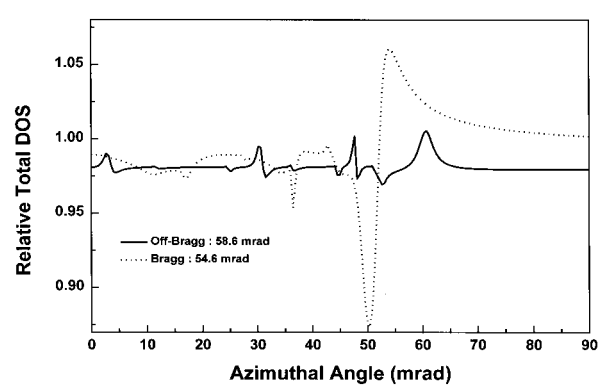

Fig. 12. The specular total DOS for glancing angles 58.6 mrad and 54.6 mrad.

for (*b*). In both Figs. 11(*a*) and (*b*), the remnants of such a structure is observed. Also, the surface resonance structure is clearly evident for both Bragg and off-Bragg scattering geometries, and in the case of the ($\bar{2}$20) mode there is little difference (apart from peak shift) between them. This is however untrue for the specular total relative DOS. Fig. 12 displays the specular total relative DOS at a more appropriate scale, revealing that the specular DOS is significantly altered and enhanced at the surface resonance condition when under the Bragg scattering geometry. Comparison with the corresponding reflection coefficients (Figs. 5 and 6) indicates clear similarities. Indeed, all features are detailed in both the total *specular* relative DOS and the reflection coefficients demonstrating the strong relationship between scattering modes and the associated availability of specular mode electronic states.

6. Discussion and concluding remarks

Figs. 7 and 8 display the local DOS at the (111) surface layer for the ($\bar{2}$20) scattering mode. As already indicated in the previous section, the one-rod calculation of the evanescent Green's function is clearly a poor approximation to that produced by the two-rod calculation [(000) and ($\bar{2}$20)]. However, the existence of the surface-resonance peak in the one-rod case demonstrates that, fundamentally, the origin of the surface resonance phenomenon lies in the potential scattering of the ($\bar{2}$20) evanescent mode. When coupled with the specular mode, as in the two-rod calculation, the corresponding pole of the evanescent Green's function is modified along with its residue to produce the observable surface-resonance peak in the specular reflection coefficient.

The position and height of the surface resonance peak (Figs. 5 and 6) in the reflection spectra differ slightly from those of Dudarev & Whelan (1994*a*,*b*, 1995, 1996). This observation reveals that the form of the evanescent Green's function originally chosen by Dudarev & Whelan for their analytical two-rod calculation must implicitly arise from a first-principles *many-rod* calculation, rather than a single-rod calculation of the ($\bar{2}$20) mode. This is in fact the case, since to determine the pole structure of their resonant Green's function, a 31-beam calculation was used to investigate the nature of the bulk (narrow) band contributing to the surface-resonance peak. This approach of choosing a form of the Green's function which already contains many-rod effects is reminiscent of Bethe's early two-beam renormalized potential procedure (Bethe, 1928) commonly referred to as 'Bethe potentials' (Cowley, 1990), in which the off-diagonal elements of the two-beam problem implicitly included many-beam effects.

Figs. 7 and 8 also demonstrate that in a two-rod calculation the ($\bar{2}$20) local DOS is largely independent of whether the specular mode satisfies a Bragg or off-Bragg condition. The local ($\bar{2}$20) DOS peaks corresponding to the surface resonance only shift due to the changed incident electron direction, but otherwise are identical, indicating that the nature of the dynamical coupling between the ($\bar{2}$20) and (000) modes is insensitive to whether the scattering is coherent or incoherent in the specular mode. This suggests that the form of an evanescent Green's function coupled to a specular mode remains essentially intact, regardless of whether the specular component intersects a horizontal Kikuchi line or not. This is further confirmed through Figs. 9 and 10, where the spatial distribution of ($\bar{2}$20) electronic states is also shown to be independent of the nature of potential scattering of the specular mode.

Although in Figs. 9 and 10 the ($\bar{2}$20) states are clearly localized at the (111) planes, the present technique does not provide information about the nature of these states. That is, whether they admit hopping between the (111) planes. Such 'transport' information can only be obtained by investigating the form of the Green's function connecting two (111) planes. In the case of the one-rod calculation, we know that the states are localized due to the evanescent nature of the homogeneous Green's function. However, in the case of the two-rod calculation where indeed the peaks about the planes have been significantly broadened, no direct information can be gained on interplane hopping dynamics using the local DOS methods.

In Fig. 11, the total relative DOS using a two-rod calculation for both the specular and the ($\bar{2}$20) mode reveal that in the latter the total relative DOS in the evanescent regime is largely unaffected by Bragg/off-Bragg scattering geometries. We note, however, that the specular total DOS is significantly affected. Furthermore, the ($\bar{2}$20) mode is also changed when in the propagating regime, *i.e.* when the corresponding side beam emerges from the solid. Fig. 12 reveals how greatly the specular mode is affected by the Bragg/off-Bragg conditions, just as in the case of the reflection coefficients shown in Figs. 5 and 6. In Fig. 12, the significant change in shape of the total relative DOS resonance peak, when comparing the off-Bragg and the Bragg conditions, is due to the interference between the resonant and the potential scattering contribution. Indeed, Dudarev & Whelan (1997) have demonstrated that, in the case of purely potential scattering, the peaks in the reflectivity associated with horizontal Kikuchi lines correspond to forbidden gaps within the total DOS.

In the present paper, we have outlined a physically transparent real-space approach to calculating the *n*-rod reflection coefficients and both the local and total density of states for an arbitrary semi-infinite material. These techniques allow a first-principles determination of the electronic Green's function for each individual scattering mode as well as off-diagonal Green's-function scattering amplitudes. By virtue of the Green's-function perspective, the iterative solution of the *n*-rod problem

requires as its primary numerical algorithm the inversion of complex symmetric matrices – in most cases, a numerically stable procedure. Application to Pt(111) of these numerical techniques using a simple two-rod approximation reveals that the resonant (evanescent) Green's-function structure is essentially independent of the nature of specular scattering, whereas the specular Green's function, like that of the corresponding reflection coefficient, is strongly dependent on it. In conclusion, the methods outlined in this work further support the usage of the local and total density of states as a tool to investigate the dynamical process of RHEED and that traditional Green's function/diagrammatic methods provide a lucid insight into their nature and determination.

The authors acknowledge the financial assistance of the Australian Research Council Small Grant Scheme. AES thanks Professor Alex Moodie and Dr Denis Lynch for their considerable help and friendly advice in the understanding of dynamical electron diffraction from surfaces.

References

Bethe, H. (1928). *Ann. Phys. (Leipzig)*, **87**, 55–129.
Cowley, J. M. (1990). *Diffraction Physics*, 2nd ed., ch. 8.6. Amsterdam: Elsevier.
Derlet, P. M. & Smith, A. E. (1997). *Phys. Rev. B*, **55**, 7170–7181.
Dudarev, S. L. & Whelan, M. J. (1994*a*). *Surf. Sci.* **310**, 373–389.
Dudarev, S. L. & Whelan, M. J. (1994*b*). *Phys. Rev. Lett.* **72**, 1032–1035.
Dudarev, S. L. & Whelan, M. J. (1995). *Surf. Sci.* **340**, 293–308.
Dudarev, S. L. & Whelan, M. J. (1996). *Int. J. Mod. Phys.* B**10**, 133–168.
Dudarev, S. L. & Whelan, M. J. (1997). *Acta Cryst.* A**53**, 63–73.
Economou, E. N. (1983). *Green's Functions in Quantum Physics*, 2nd ed., ch. 1. Berlin: Springer-Verlag.
Peng, L.-M. (1994). *Surf. Sci.* **316**, L1049-L1054.
Smith, A. E., Lehmpfuhl, G. & Uchida, Y. (1992). *Ultramicroscopy*, **41**, 367–373.
Wang, Z. L. (1995). *Elastic and Inelastic Scattering in Electron Diffraction and Imaging*, pp. 85–87. New York/London: Plenum Press.
Wang, Z. L. (1996). *Reflection Electron Microscopy and Spectroscopy for Surface Analysis*, ch. 3. Cambridge University Press.